A&A, 684, A90 (2024)
https://doi.org/10.1051/0004-6361/202347083

Astronomy & Astrophysics

Unveiling the journey of a highly inclined CME

Insights from the March 13, 2012, event with 110° longitudinal separation

F. Carcaboso[1,2,3], M. Dumbović[4], C. Kay[2,3], D. Lario[2], L. K. Jian[2], L. B. Wilson III[2], R. Gómez-Herrero[5], M. Temmer[6], S. G. Heinemann[7], T. Nieves-Chinchilla[2], and A. M. Veronig[6,8]

[1] NASA Postdoctoral Program Fellow, NASA Goddard Space Flight Center, Greenbelt, MD, USA
e-mail: fernando.carcabosomorales@nasa.gov
[2] Heliophysics Science Division, NASA Goddard Space Flight Center, Greenbelt, MD, USA
[3] Physics Department, The Catholic University of America, Washington, DC, USA
[4] Hvar Observatory, Faculty of Geodesy, University of Zagreb, Kaciceva 26, 10000 Zagreb, Croatia
[5] Universidad de Alcalá, Space Research Group (SRG-UAH), Plaza de San Diego s/n, 28801 Alcalá de Henares, Madrid, Spain
[6] Institute of Physics, University of Graz, Universitätsplatz 5, 8010 Graz, Austria
[7] Department of Physics, University of Helsinki, PO Box 64, 00014 Helsinki, Finland
[8] Kanzelhöhe Observatory for Solar and Environmental Research, University of Graz, Austria

Received 2 June 2023 / Accepted 20 January 2024

ABSTRACT

Context. A fast (~2000 km s^{-1}) and wide (>110°) coronal mass ejection (CME) erupted from the Sun on March 13, 2012. Its interplanetary counterpart was detected in situ two days later by STEREO-A and near-Earth spacecraft, such as ACE, Wind, and Cluster. We suggest that at 1 au the CME extended at least 110° in longitude, with Earth crossing its east flank and STEREO-A crossing its west flank. Despite their separation, measurements from both positions showed very similar in situ CME signatures. The solar source region where the CME erupted was surrounded by three coronal holes (CHs). Their locations with respect to the CME launch site were east (negative polarity), southwest (positive polarity) and west (positive polarity). The solar magnetic field polarity of the area covered by each CH matches that observed at 1 au in situ. Suprathermal electrons at each location showed mixed signatures with only some intervals presenting clear counterstreaming flows as the CME transits both locations. The *strahl* population coming from the shortest magnetic connection of the structure to the Sun showed more intensity.
Aims. The aim of this work is to understand the propagation and evolution of the CME and its interaction with the surrounding CHs, to explain the similarities and differences between the observations at each spacecraft, and report what one of the most longitudinal expanded CME structures measured in situ would be.
Methods. Known properties of the large-scale structures from a variety of catalogues and previous studies were used to have a better overview of this particular event. In addition, multipoint observations were used to reconstruct the 3D geometry of the CME and determine the context of the solar and heliospheric conditions before the CME eruption and during its propagation. The graduated cylindrical shell model (GCS) was used to reproduce the orientation, size and speed of the structure with a simple geometry. Also, the Drag-Based Model (DBM) was utilised to understand the conditions of the interplanetary medium better in terms of the drag undergone by the structure while propagating in different directions. Finally, a comparative analysis of the different regions of the structure through the different observatories was carried out in order to directly compare the in situ plasma and magnetic field properties at each location.
Results. The study presents important findings regarding the in situ measured CME on March 15, 2012, detected at a longitudinal separation of 110° in the ecliptic plane despite its initial inclination being around 45° when erupted (March 13). This suggests that the CME may have deformed and/or rotated, allowing it to be observed near its legs with spacecraft at a separation angle greater than 100°. The CME structure interacted with high-speed streams generated by the surrounding CHs. The piled-up plasma in the sheath region exhibited an unexpected correlation in magnetic field strength despite the large separation in longitude. In situ observations reveal that at both locations there was a flank encounter – where the spacecraft crossed the first part of the CME – then encountered ambient solar wind, and finally passed near the legs of the structure.
Conclusions. A scenario covering all evidence is proposed for both locations with a general view of the whole structure and solar wind conditions. Also, the study shows the necessity of having multipoint observations of large-scale structures in the heliosphere.

Key words. methods: data analysis – Sun: corona – Sun: coronal mass ejections (CMEs) – solar-terrestrial relations – solar wind

1. Introduction

Coronal mass ejections (CMEs) are large expulsions of plasma originating from the Sun, commonly resulting from processes of magnetic instabilities and reconnection in the solar corona. These structures are constituted by a strongly magnetised plasma which usually remains defined until several astronomical units (e.g. Witasse et al. 2017) as they propagate quasi-radially outwards from the Sun covering a considerable angular extent. Occasionally, the placement of different spacecraft in the heliosphere is appropriate to measure in situ the passage of CMEs at different heliospheric locations. The combination of the corresponding measurements by spacecraft at different heliospheric locations is referred to as multipoint observations. These

multipoint observations allow a better understanding of the global and local topology of the large-scale structures, as well as their evolution and possible interaction with the surrounding medium, as well as with other solar wind (SW) structures (e.g. Möstl et al. 2009; Winslow et al. 2016).

The interplanetary counterparts of CMEs are usually divided into distinguishable parts sequentially observed in the following order (e.g. Rouillard 2011):

– *Shock.* It can be recognised by abrupt plasma parameters increase (Krall 1997). Depending primarily on the CME speed relative to the upstream SW. In the case of subsonic or sub-Alfvenic speeds, the shock cannot form.

– *Sheath.* Not all CMEs develop sheaths (see e.g. Liu et al. 2006; Salman et al. 2020). The ambient SW piles up around the CME, compressing it, resulting in an irregular and turbulent plasma and magnetic field. Typically, sheath crossings last ∼10 h at 1 au (Temmer & Bothmer 2022).

– *Magnetic obstacle or ejecta.* This region has an intense magnetic field and commonly few plasma fluctuations. It can be a pre-existing flux rope (FR) or be formed during the eruption of the CME (Zurbuchen & Richardson 2006; Richardson & Cane 2010; Nieves-Chinchilla et al. 2019). It may also present single or multiple FRs or none. If there is(are) FR(s) showing additional properties such as low plasma β or bidirectional suprathermal electrons (BDEs), it is often denominated as a magnetic cloud (MC, Burlaga et al. 1981; Gosling et al. 1987).

– *Post-CME.* After the magnetic obstacle transit, a loosely defined region exists, with mixed characteristics from ambient SW and CME (Vršnak et al. 2009). Signatures such as BDEs can still be found (Carcaboso et al. 2020). Their duration at 1 au can last longer than the actual CME transit (Rodriguez et al. 2016; Temmer et al. 2017; Carcaboso et al. 2020).

Previous studies such as Vourlidas et al. (2017) provide some statistics about the properties of the CMEs and estimate that the average angular width of these structures increases with the solar cycle, reaching ∼80° as maximum. There are also case-study articles that broadened our knowledge about the complexity of the CMEs, often with the combination of remote sensing observations and in situ measurements. Sometimes, these large-scale structures are captured in situ by multiple spacecraft separated in longitude, which helps to understand the global topology and their inherent dynamics, as well as the interaction with the surrounding SW or other structures. For example, the following studies sorted in longitudinal angular separation analysed different events: Lugaz et al. (2022), 55°; Liu et al. (2008), 74°; Rodríguez-García et al. (2021), 80°; Chen et al. (2022), 90°, and Richardson et al. (2002), 160°. On those lines, Winslow et al. (2022) describe the importance of the multipoint analysis to understand these large-scale structures in the SW, while Scolini et al. (2023) theorise about the amount of spatially separated spacecraft needed for their complete understanding and characterisation.

Often, the presence of coronal holes (CHs) surrounding the region where CMEs originate, and the SW streams emanating from them (usually, high-speed SW streams) may play a significant role in their propagation. For example, they could act as 'magnetic walls' that hamper their propagation (Gopalswamy et al. 2009). The interaction between CMEs and high-speed SW streams can lead to significant changes in CME properties during their journey through the heliosphere, for example, forcing the internal structure of the CMEs to deform, deflect, kink or rotate (Riley & Crooker 2004; He et al. 2018; Chen et al. 2019; Geyer et al. 2023). Also, high-speed streams could potentially accelerate CMEs, shortening their propagation time from the Sun to Earth (Cargill et al. 1996; Vršnak 2001; Vršnak & Gopalswamy 2002).

A very fast and wide CME erupted from the Sun on March 13, 2012. We discuss the possibility that its interplanetary counterpart was detected in situ two days later by spacecraft located close to Earth – particularly, by the European Space Agency's (ESA's) Cluster (Escoubet et al. 2001), and the National Aeronautics and Space Administration's (NASA's) Wind (Ogilvie & Desch 1997; Wilson et al. 2021) and the Advanced Composition Explorer (ACE, Stone et al. 1998) – as well as by the Ahead spacecraft of the NASA's Solar Terrestrial Relations Observatory (STEREO-A, Kaiser et al. 2008). We present a scenario where Earth intercepted the east flank of the CME, whereas STEREO-A, separated by 110° in longitude with respect to Earth, crossed the west flank. Despite the large longitudinal separation between STEREO-A and Earth, measurements from both positions showed similar in situ CME signatures, especially during the passage of the leading and rear regions of the CME transit at both locations. When the CME was released from the Sun, three CHs were observed surrounding the active region (AR) where the CME originated, resulting in a particular propagation behaviour of this structure towards the different observatories.

This study aims to explain the propagation and topology of this extremely broad CME released from the Sun on March 13, 2012, and its interaction with the surrounding CHs, using both remote-sensing observations and in situ measurements. Section 2 shows the evidence from the images provided by the different observatories, and Sect. 3 shows the local SW properties during the arrival and crossing of the CME. Section 4 describes the application of different methodologies supporting the hypothesis that the observed structure resulted from the same solar eruption and were in fact the same CME despite the large longitudinal separation of the locations where the in situ measurements were taken. Section 5 outlines a possible scenario consistent with the observations. Finally, Sect. 6 summarises the work and Sect. 7 discusses the results implied by the scenario that reconstructs the observations.

2. Remote-sensing observations

The locations in the heliosphere of both STEREO spacecraft (STEREO-A and STEREO-B) and near-Earth spacecraft in March 2012 enabled remote-sensing observations that covered the entire Sun in longitude, and thus provided a perfect opportunity to analyse CME structures propagating away from the Sun. The orbital configuration of the spacecraft can be seen in Fig. 1, whereas the coordinates of the spacecraft used in this study, are listed in Table 1. The instruments used for the remote-sensing observations are listed in Appendix A. In the following subsections, the solar-corona conditions and part of the propagation of the CME captured by the remote-sensing instruments are described.

2.1. Solar flare and CME

The CME under analysis occurred during the rising phase to the solar maximum of solar cycle 24, with multiple events occurring hours before and after (e.g. Tsurutani et al. 2014; Su et al. 2015). Noteworthy is the CMEs on March 7, which erupted from the same AR as the CME under analysis and caused a widespread solar energetic particle (SEP) event that has been analysed in detail from different approaches (e.g. Lario et al. 2013;

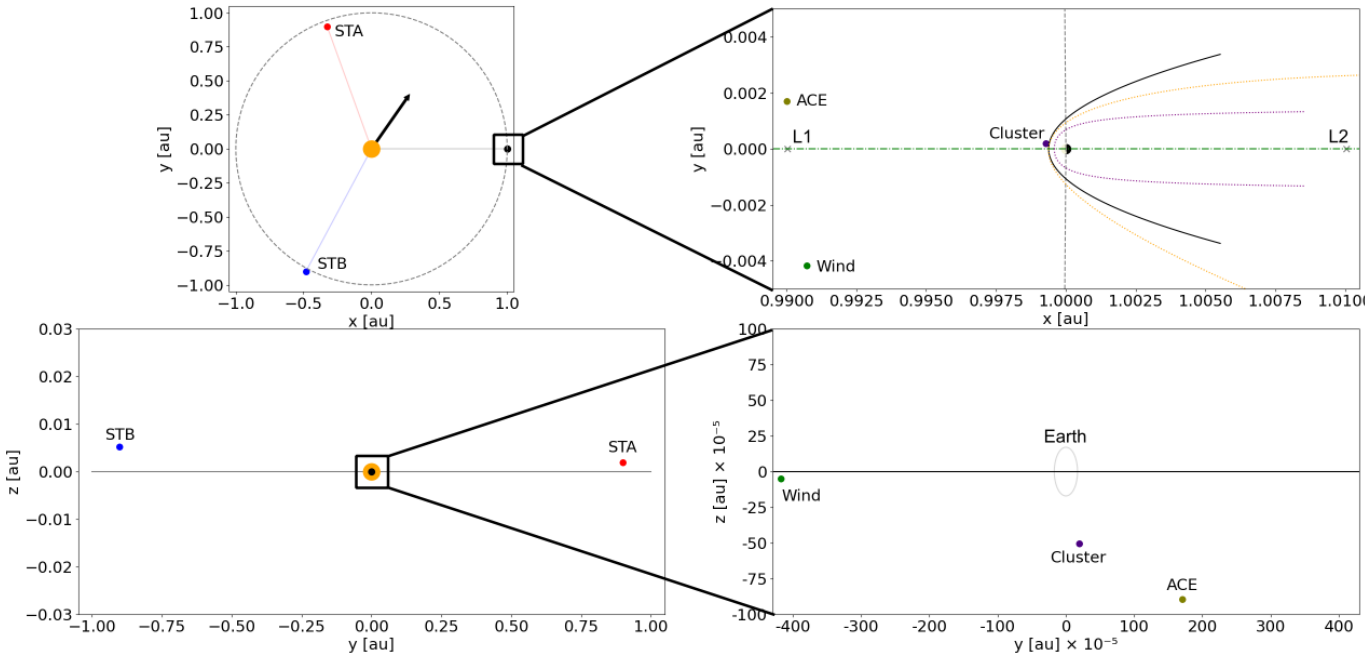

Fig. 1. Orbital configuration in HEE coordinates of the analysed spacecraft during the event. Black arrow shows the longitude of the AR at the moment of the eruption. Earth's magnetospheric bow shock (orange) and magnetopause (purple) are calculated as in Ipavich et al. (1981) with a speed of 500 km s^{-1} (black line indicates the bow shock without the influence of the SW). Crosses in Earth's perspective indicate the Lagrange points. Earth's radius is scaled by a factor of 4. Sun not to scale. The x, y, and z scales are different in some of the panels.

Table 1. Mean orbital position of the spacecraft in heliocentric Earth-ecliptic (HEE) coordinate system during the dates March 14, 2012, and March 20, 2012, sorted by longitude, where ϕ is longitude, θ is latitude, and r is heliocentric radial distance.

s/c	ϕ [deg]	θ [deg]	r [au]
STEREO-B	-118.27 ± 0.12	0.29 ± 0.00	1.02
Wind	-0.24 ± 0.00	0.00 ± 0.01	0.99
Cluster	0.01 ± 0.02	-0.02 ± 0.02	1.00
ACE	0.10 ± 0.00	-0.05 ± 0.00	0.99
STEREO-A	110.12 ± 0.21	0.10 ± 0.00	0.96

Notes. Uncertainties correspond to the maximum variation during that period (r did not vary significantly).

Patsourakos et al. 2016; Feng et al. 2020; Hudson et al. 2023; Soni et al. 2023).

Preceding the main CME analysed in this paper, there is a small event seen in STEREO-A/EUVI that happened on March 13 at approximately 15:34 UT from AR11430 located at N22W81 as seen from Earth (catalogued by the National Oceanic and Atmospheric Administration, NOAA, Space Weather Prediction Center, SWPC). This small previous eruption might have triggered the flare and CME eruption under study in this paper due to global instabilities related to large eruptions (for example, waves, magnetic pressure change, etc.). The full coverage in longitude of the Sun provided by the different spacecraft thanks to their orbital position allows us to confirm that there were no other potential CMEs in the direction of Earth or STEREO-A in a period of 24 h prior to and after the occurrence of the main CME studied here.

The main CME under study is related to an M7.9 X-ray solar flare from AR11429 at N18W64 (NOAA/SWPC) with the onset of the soft X-ray emission on March 13 at 17:12 UT. The longitude of this AR is indicated by the black arrow in the top left panel of Fig. 1. The CME was first observed by SOHO/LASCO/C2 at 17:36 UT, and by both STEREO-A and STEREO-B COR1 at ~17:30 UT (see Sect. 4.1 for more details). The AR configuration was classified as a complex $\beta\gamma\delta$ (see Jaeggli & Norton 2016, and references therein for a detailed explanation). Prior to this event, the AR was very dynamic, with multiple CME eruptions (see e.g. Liu et al. 2013, 2014b; Dhakal et al. 2020)[1].

Palmerio et al. (2018) determined that the CME on March 13 had a left-handed helicity as derived from different multi-wavelength proxies (i.e. magnetic tongues X-ray/EUV sigmoids, the skew of coronal arcades, flare ribbons, and filament details; see also Palmerio et al. 2017 and references therein). Harker & Pevtsov (2013) describe in detail the magnetic conditions during the eruption, and the appearance of a magnetic transient during the flare.

The CME was observed from different white light coronagraphs, appearing as a backside halo CME from STEREO-B's perspective, that is, moving in the opposite direction of the spacecraft with a main northward propagation. STEREO-A and SOHO observed the CME propagating in the north-east and northwest directions, respectively. STEREO-A/HI and STEREO-B/HI data provided valuable observations of the eastern and western flanks of the wide CME during its heliospheric propagation. The first observation of the structure in STEREO-A/HI and STEREO-B/HI occurred at 18:49 UT and 19:29 UT on March 13, respectively, and was catalogued as *HCME_B__20120313_01* and *HCME_A__20120313_01* by the Heliospheric Cataloguing, Analysis and Techniques Service

[1] Images of the event provided by SDO/AIA can be found under the following link: https://sdowww.lmsal.com/sdomedia/ssw/media/ssw/ssw_client/data/ssw_service_120313_105302_91045/www

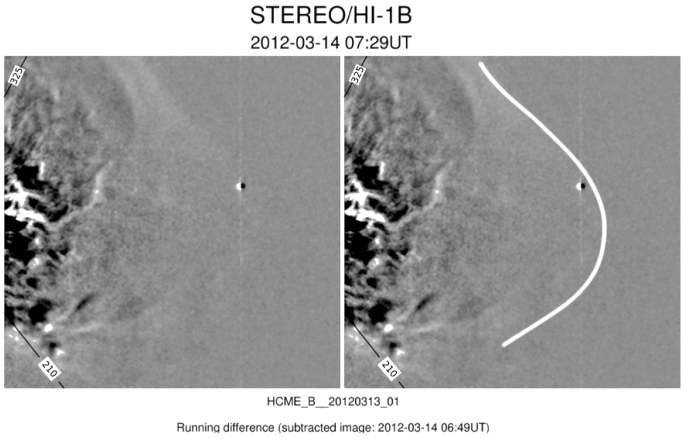

Fig. 2. Running difference image from STEREO-B/HI observed on March 14 at 07:29 UT. White line at the right panel indicates approximately the leading edge of the CME. Captured planet (brightest point) corresponds to Mercury. Adapted image from HELCATS.

(HELCATS)[2]. As seen by STEREO-B/HI, the northern position angle of the CME span was >325°, while the southern was 210°. By March 14 at 07:29 UT, the CME's propagating structure showed some distortion on its leading edge, particularly in the northern section, as indicated in the right panel of Fig. 2.

As a first estimate, extracted from the propagation directions in the coronagraphs and STEREO/HI observations, the CME propagated in the region between Earth and STEREO-A. As reported by HELCATS, the shock speed derived from the Jmap (Davies et al. 2009) is around $1050 \pm 450\,\mathrm{km\,s^{-1}}$. HELCATS also estimates an arrival time at Earth on March 15 at 12:28 UT and with a speed of $850\,\mathrm{km\,s^{-1}}$, which differs by $50\,\mathrm{km\,s^{-1}}$ for the speed and ~35 min in advance of the actual arrival time (see ACE, Wind and Cluster observations in Sect. 3 and Table 2 below for more detailed information).

2.2. Coronal holes overview

Three CHs, apart from the northern polar CH, were located surrounding the parent AR. The properties of the CHs were analysed using the programme Collection of Analysis Tools for Coronal Holes (CATCH, Heinemann et al. 2019b). In Fig. 3, their locations with respect to the parent AR (indicated by a purple ellipse) can be seen. The eastern one (CH1, red) had inward (negative) magnetic polarity, while the southwest (CH2, green) and west (CH3, blue) CHs had outward (positive) magnetic polarity. At the moment of the eruption, each CH had the following properties:

– CH1 was the largest among the three, covering a total area of $\sim 12 \times 10^{10}\,\mathrm{km^2}$, with its centre of mass at approximately −3° in latitude and −3° in longitude (Stonyhurst coordinates; the reference system is different from the one shown in Fig. 3). This CH has been studied in more detail, providing information on its evolution and properties by Heinemann et al. (2018a,b).

– CH2 covered an area of $\sim 4.5 \times 10^{10}\,\mathrm{km^2}$, and it is the furthest one with respect to the AR, with its centre of mass located at −36° (latitude), 99° (longitude).

– CH3 is the smallest CH, covering an area of $\sim 3 \times 10^{10}\,\mathrm{km^2}$ at the moment of the eruption. Its centre of mass was located at 29° (latitude), 132° (longitude).

EUV images also show the presence of a diffused region surrounding CH2 and CH3. Due to this reason and the fact that both of them share the same polarity, it could be argued that these two CHs are darker regions within the same large and less-defined CH.

The presence of a low coronal shock wave produced by the CME (see Sect. 2.1) that clearly interacted with the CHs can be easily observed in the SDO/AIA multi-wavelength composed image[3]. CH1 acted as a barrier hampering the propagation of the shock to further eastern distances, and the boundaries of them are reflected in the video. Figure 4 shows a snapshot of that moment at 17:53 UT on March 13, when the EUV wave reflection with CH1 is clearly observed (the red arrows mark the boundaries of CH1, while the pink arrow marks the AR site where the flare occurred). Due to the clear features of this EUV wave and its size, although beyond the scope of this study, a more detailed analysis of the remote-sensing observations of this event in the lower corona is encouraged.

3. In situ observations

Two days after the eruption of the CME, a shock associated with a CME was detected in situ by STEREO-A and by near-Earth spacecraft with a relatively short time difference. At that time, STEREO-A was located at 0.96 au from the Sun and separated 110° west from Earth (see Fig. 1). In the following subsections, the interplanetary context and the plasma properties during the transit of the relative crossings measured at the different locations are described. The in situ instruments utilised for this purpose are listed in Appendix A. All the represented data have been acquired from the NASA's Coordinated Data Analysis Web (CDAWeb[4]), part of the Space Physics Data Facility (SPDF).

3.1. Near-Earth observations

Earth's surrounding ambient SW properties were measured by Wind, ACE and the four spacecraft of the Cluster mission. All these spacecraft detected similar time profiles of the magnetic field and plasma parameters (with the exception of Cluster's magnetospheric crossing). Figure 5 shows the in situ plasma and magnetic field parameters observed by ACE[5] (left) and Wind[6] (right) between March 14 (day of year 74) and March 20 (day of year 80), 2012. The panels show from top to bottom: SW bulk speed, proton density, kinetic proton temperature (blue and orange) together with an empirically predicted temperature (yellow) based on the proton speed as explained in Lopez (1987) and Elliott et al. (2012), magnetic field strength, its vector components in the spacecraft-centred radial-tangential-normal (RTN) coordinates, the azimuthal angle in the RTN coordinate system (deg) complemented with the two possible nominal Parker spiral angles calculated from the proton speed and accompanied by

[2] https://www.helcats-fp7.eu/catalogues/data/HCME_WP2_V06.txt

[3] https://suntoday.lmsal.com/sdomedia/SunInTime/2012/03/13/AIAtriratio-211-193-171-2012-03-13T1200.mov.mp4

[4] https://cdaweb.gsfc.nasa.gov

[5] During this period, SWEPAM only provided SW speed. SW density and temperature are obtained from SWICS, whereas the total pressure and the plasma β parameter are computed using SWICS and ACE/MAG data.

[6] SW plasma parameters are obtained from 3DP (orange) and SWE (blue) data resampled to 1-min cadence. 3DP density was multiplied by a factor of 5 to be comparable with the other sensors. Due to the low values of density as measured from 3DP, temperature measurements are inaccurate. For this reason, temperature, density and their derivatives from 3DP have not been used for the analysis.

Table 2. Start, end, and duration of the different regions of the in situ measured CME based on changes in the tendency of the SW speed for the different spacecraft. Last column compares the duration of the different regions at each spacecraft with respect to Wind.

s/c	Region	Start (March 2012) (day HH:MM UT)	End (March 2012) (day HH:MM UT)	Duration (min.)	Δt wrt Wind (min.)
Wind	#1	15 12:34	15 15:48	194	–
	#2	15 15:48	15 20:46	298	–
	#3	15 20:46	16 09:14	748	–
	#4	16 09:14	16 14:21	308	–
	#5	16 14:21	16 23:52	570	–
	#6	16 23:52	17 21:57	1325	–
	#7	17 21:57	18 03:13	316	–
	#8	18 03:13	18 11:08	475	–
	A	18 11:08	19 03:30	982	–
ACE	#1	15 12:32	15 15:40	188	−6
	#2	15 15:40	15 21:03	323	+25
	#3	15 21:03	16 08:12	669	−79
	#4	16 08:12	16 14:27	375	+67
	#5	16 14:27	16 22:32	485	−85
	#6	16 22:32	17 22:00	1408	+83
	#7	17 22:00	18 03:11	311	−5
	#8	18 03:11	18 10:19	428	−47
	A	18 10:19	19 03:09	1010	+28
Cluster 1	Magnetosphere	<15 00:00	15 04:12	–	–
	#1	15 13:08	15 16:27	199	+5
	#2	15 16:27	15 21:53	326	+28
	Interaction	15 21:53	16 05:09	436	–
	Magnetosphere	16 05:09	17 00:15	1146	–
	Interaction	17 00:15	17 20:04	1189	–
	#6	17 20:04	17 21:50	106(*)	–(*)
	#7	17 21:50	18 03:32	342	26
	Interaction	18 03:32	18 08:24	291	–
	Magnetosphere	18 08:24	19 06:54	1351	–
STA	#1	15 22:29	16 00:44	135	−59
	#2	16 00:44	16 09:04	314	−16
	#3	16 09:04	16 16:48	463	−350
	#4	16 16:48	16 21:11	263	+20
	#5	16 21:11	16 23:56	165	−405
	#6	16 23:56	17 14:14	858	−467
	#7	17 14:14	17 20:54	400	+84
	#8	17 20:54	18 06:22	568	−414

Region	Description
#1	It starts with the shock and forms part of the sheath region.
#2	It is defined between a sudden enhancement of the bulk speed and the sudden depletion of this physical property. It is partially covering the sheath, and from the near-Earth observations, part of the magnetic obstacle of the structure too.
3	Expanding region. It has a clear FR structure at Earth, but not at STEREO-A. For Earth, it can be considered as a magnetic cloud (Nieves-Chinchilla et al. 2019), while for STEREO-A is considered part of the sheath (Jian et al. 2018).
#4	Increasing speed from ∼625 to ∼700 km s^{-1} at Earth, and from ∼425 to ∼500 km s^{-1} at STEREO-A.
#5	The speed profile presents a 'u' shape or parabola behaviour.
#6	Speed remains more or less constant with a very fluctuating behaviour.
#7	It shows a gradual decrease of the speed with smooth behaviour for the three s/c, indicating an expansion. The magnetic field strength matches for all the observers.
#8	Expanding region.
A	Expanding region ending with a bulk speed plateau that ends up in a SIR (observed only near Earth).
Interaction	It is a mixture of the magnetopause and the transit of the in situ CME.

Notes. (*)Comparison to Wind is not possible due to the previous interaction with the magnetosphere.

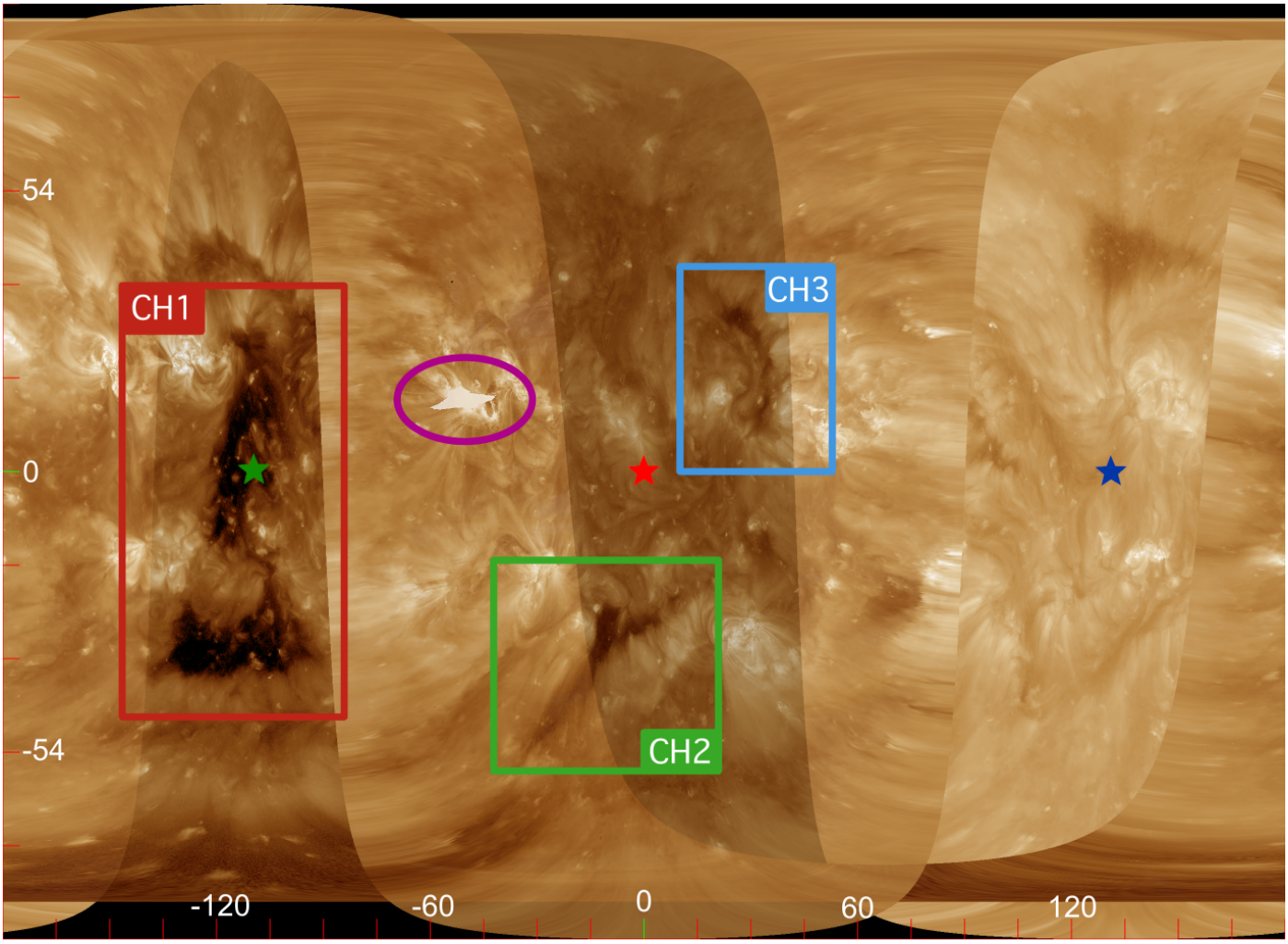

Fig. 3. Projection of a composed image from SDO/AIA 193 Å, STEREO-A and STEREO-B EUVI 195 Å at the moment of the solar flare preceding the CME release. The axes correspond to latitude and longitude (in degrees) as seen from STEREO-A in the ecliptic plane. Purple ellipse shows the AR, while the red, blue, and green boxes indicate the surrounding CHs. Stars represent the projection of each location (green, Earth; red, STEREO-A; blue, STEREO-B). See text for more details.

its polarity (red, negative; green, positive; yellow, ambiguous)[7], interplanetary magnetic field latitudinal angle in the RTN coordinate system, total pressure[8], and plasma β.

The shaded areas indicate different regions based on identifiable bulk speed features, which are associated with different conditions of the SW during the passage of the CME and which may differ from the four distinguishable parts explained in Sect. 1 (see Sect. 4.3 and Table 2 for more details). The SW conditions preceding the arrival of the CME show no remarkable features, with a SW speed of ~500 km s^{-1}, low density, and constant negative (inward) polarity, almost following the nominal Parker spiral. The vertical black dashed line indicates the passage of the shock associated with the CME. The shock reaches ACE at 12:31 UT on March 15 (day of year 75), similar to Wind's time (12:33 UT). The shock parameters are estimated solving numerically the Rankine-Hugoniot relations (e.g. Viñas & Scudder 1986; Koval & Szabo 2008) using the Space Plasma Missions IDL Software Library (Wilson 2022). For Wind, the analysis found a quasi-perpendicular shock (the angle between the upstream magnetic field and the normal to the shock, θ_{BN}, was 76.2° ± 0.7°) with a normal vector ⟨−0.771, −0.538, −0.340⟩ ± ⟨0.007, 0.005, 0.008⟩ in GSE coordinates (uncertainties are due to statistical errors only; they do not include systematic errors or proper measurement errors), and a fast magnetosonic Mach number of ~3.1.

After the MC, a region with more or less stable SW (with a speed of around 600 km s^{-1}) can be found. This region covering the periods #4, #5, and #6 in Fig. 5 shows higher temperature and lower magnetic field strength (and consequently, higher plasma β) than the MC. The period is divided into three different parts based on the trend of the SW speed. However, the suprathermal electron pitch-angle distributions (PADs; see Sect. 4.4) show a faint patchy presence of BDEs. This region is more likely to be part of the ambient SW, although there are features that may be

[7] Nominal Parker spiral angle in the ecliptic plane is calculated as $\phi = arctan(\Omega \cdot r/V_{sw})$, being $\Omega = 2.87 \times 10^{-6}$ s^{-1}. The polarities are determined with a span of ±60° with respect to the theoretical vectors.

[8] Total pressure is calculated as the addition of the plasma thermal pressure (P_g) plus the magnetic field pressure (P_B). P_g is computed as $P_g = N_p K T_p + N_e K T_e + N_{He} K T_{He}$, where $p \equiv$ protons, $e \equiv$ electrons, He ≡ helium; N corresponds to density, K to the Boltzmann constant, and T to the temperature. T_e and an alpha/proton ratio are considered constant with a value of 140 000 K and 0.04 respectively (Bürgi 1992; Newbury 1996; Mullan & Smith 2006). P_B is computed as $P_B = B^2/2\mu_0$, being B the magnetic field strength, and μ_0 the vacuum magnetic permeability.

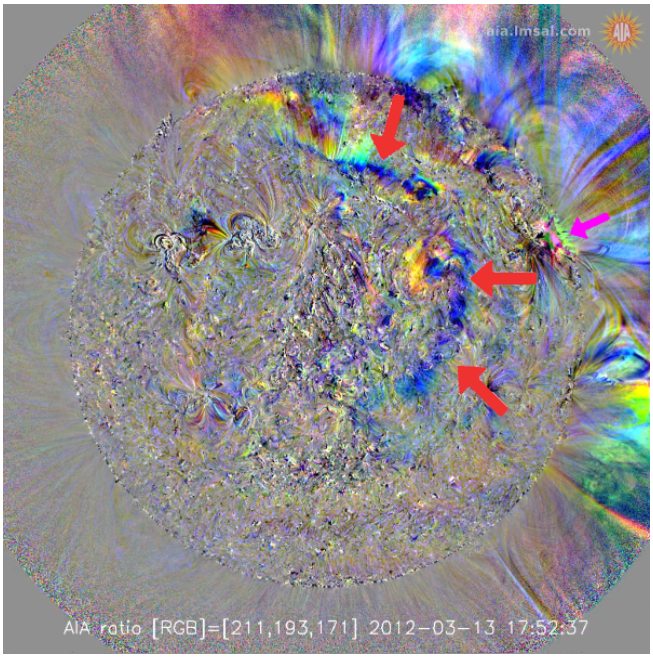

Fig. 4. Composed running difference image from SDO/AIA 211 Å, 193 Å, and 171 Å observed on March 13 at 17:52:37 UT. Red arrows indicate the appearance of the boundary of CH1 revealed by the interaction with the CME shock wave. The pink arrow points to the AR where the CME originated.

related to the MC. According to Tsurutani et al. (2014), these regions correspond to a high-speed stream following the CME which would have ended in region #3.

Two additional regions (#7, #8) correspond to another expanding regime of the SW, with low magnetic field, low proton density, and a variable magnetic field with a predominant negative polarity. The expansion in these two regions is more pronounced than the one in the previous region #3.

Finally, in contrast to regions #1 through #8, region A corresponds to a period for which no correspondence in STEREO-A observations was found (see Sect. 3.2). Nevertheless, this region seems to be still part of the expanding structure at Earth and to be interacting with a glancing cross of a SW stream interaction region (SIR) at the end, reduced by the interaction of fast SW generated from likely CH1 and SW left behind the CME, as discussed below. The different parts of this transit are analysed in detail and compared to other spacecraft observations in Sect. 4.3.

It is also noteworthy the presence of a previous interplanetary CME crossing Earth (not shown) from March 12 at 08:28 UT to March 14 at 02:52 UT, according to the Wind's in situ CME catalogue (Nieves-Chinchilla et al. 2018). This CME may have influenced the upstream conditions of the SW that the CME under study encountered as discussed in Sect. 4.

The four Cluster spacecraft were out of the magnetosphere during the arrival of the CME (not shown). All four spacecraft detected the shock on March 15 at ~13:08 UT (in an interval of 4.4 s between the first and last observer, 13:07:58.550 UT and 13:08:02.950 UT). Similarly to Wind and ACE, prior to the shock arrival, the SW had negative polarity with a constant magnetic field strength of approximately 6.5 nT. Again, the sheath of the CME could be subdivided into two main parts: a very variable and weak magnetic field (#1), and a stronger but rapidly decreasing field with with a smoother pointing direction (#2). The following region (#3) displays fluctuating magnetic field, but with a clear tendency to increase in strength, until the arrival to the Earth's bow shock at 21:53 UT when the four spacecraft reentered the magnetosphere. The different regions are analysed further in Sect. 4.

The passage of the CME through the Earth's environment caused a geomagnetic storm with $Kp > 5$ between 12:00 UT and 21:00 UT on March 15 and reached a minimum equatorial Dst value of −88 nT at 21:00 UT (not shown), while crossing the strongest values of the negative B_N component observed during the passage of region #2. Then, the Kp index kept a value between 3 and 4 until the first half of March 18, while the Dst was approximately on average −47 nT, and a maximum value of −28 nT for the same period. A $Kp = 4$ and Dst of ~−40 nT were reached between 03:00 and 07:00 UT on March 19, coinciding with the passage of the SIR partially covered in region A (see Fig. 5).

3.2. STEREO-A

The crossing of a CME through STEREO-A on the same day (March 15) is also recorded in different in situ CME catalogues (see for example the STEREO/IMPACT catalogue of CMEs[9], listed as the number 8 of year 2012). The criteria for selecting in situ CMEs on that particular catalogue can be found in a series of publications by Jian et al. (2006b, 2013, 2018). Figure 6 displays, using the same format as Fig. 5, the STEREO-A in situ measurements for that period.

The black-dashed vertical line at 22:33 UT on March 15 (day of year 75) indicates the passage of an interplanetary shock. Following the same procedure used for Wind (see Sect. 3.1), the orientation of the shock normal was obtained: $\langle -0.079, -0.997, -0.002\rangle \pm \langle 0.026, 0.002, 0.017\rangle$ (in GSE coordinates to be directly comparable to the shock normal estimate calculated using Wind data). θ_{BN} was very similar to the one measured at Wind ($66.5° \pm 3.7°$; in other words, a quasi-perpendicular shock), and the magnetosonic Mach number was ~2.1. We note that in contrast to near-Earth observations, the shock normal at STEREO-A was mostly in the ecliptic plane with a predominant western direction, whereas at Wind was mostly southwestern directed.

The shock is preceded by a relatively high-speed stream of ~470 km s^{-1} with positive polarity (green horizontal line in the eighth panel of Fig. 6), and previous to that, a heliospheric current sheet crossing at 21:30 UT on March 14 (day of the year 74). The increase of SW speed observed early on March 15 preceded by a period of elevated SW density and magnetic field magnitude late on March 14 can be interpreted as the arrival of a SIR, which presumably originated from CH2 or CH3, as their longitude and polarity agree with the observed features. According to the Predictive Science Inc. (PSI) magnetic back-mapping results[10] (not shown), STEREO-A is more likely connected to the northern hemisphere on March 15, where CH3 is located. The period with elevated magnetic field and density is also reported in the STEREO/IMPACT catalogue of SIRs[11] (shaded in blue). The

[9] https://stereo-ssc.nascom.nasa.gov/data/ins_data/impact/level3/
[10] https://www.predsci.com/hmi/spacecraft_mapping.php
[11] https://stereodata.nascom.nasa.gov/pub/ins_data/impact/level3/STEREO_Level3_SIR.pdf; see Jian et al. (2006a, 2019) for the selection criteria.

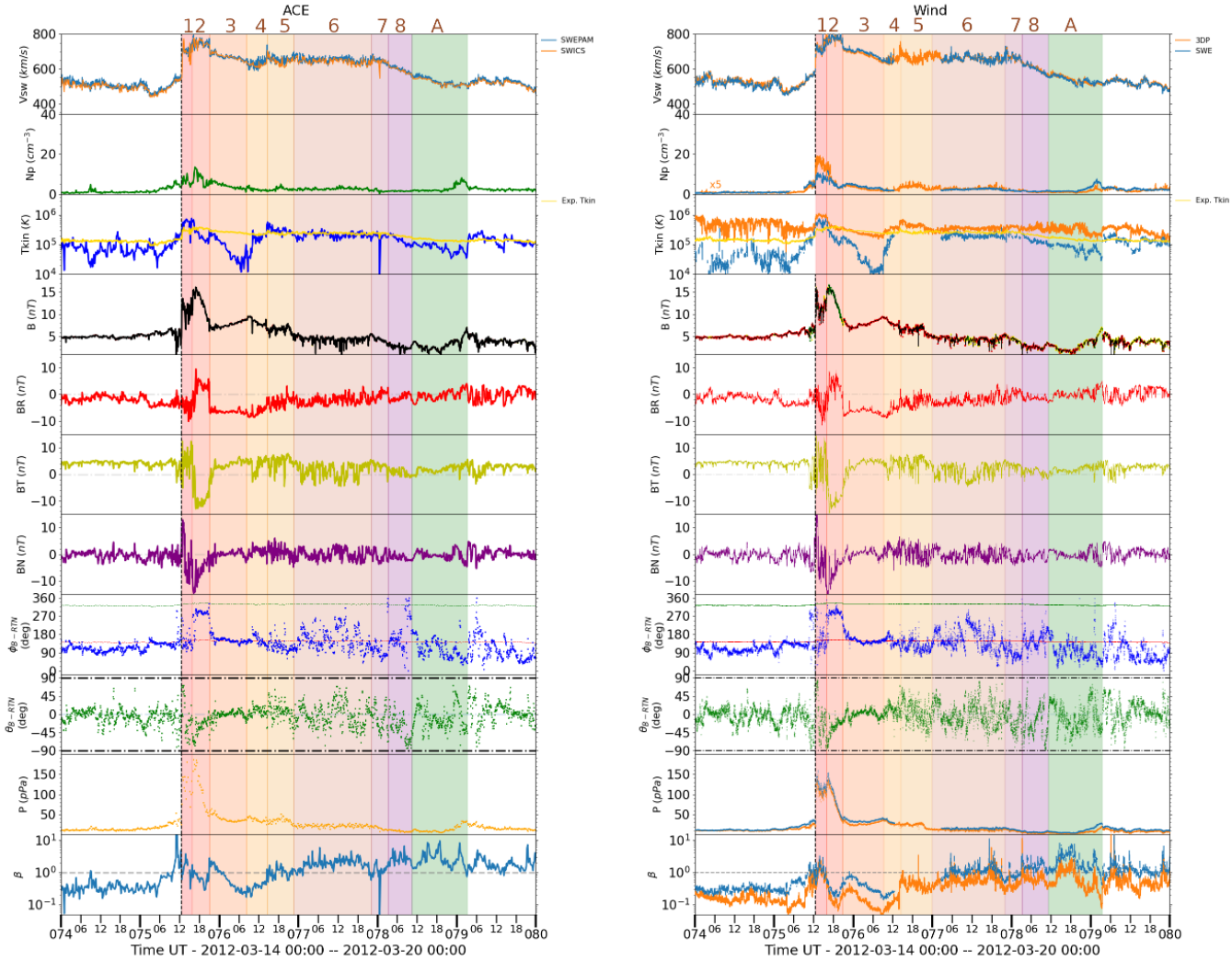

Fig. 5. ACE and Wind observations during the period from March 14, 2012, to March 20, 2012. From top to bottom: SW proton speed, proton density, proton temperature, magnetic field magnitude, magnetic field RTN components, magnetic field azimuthal angle in the RTN coordinate system complemented with the two possible nominal Parker spiral angles (red, negative; green, positive) calculated from the proton speed and accompanied by its polarity (red, negative; green, positive; yellow, ambiguous), magnetic field latitudinal angle in the RTN coordinate system, total pressure, and plasma β.

time of the stream interface passage according to the catalogue is marked by the vertical dashed grey line in Fig. 6 within that area, and corresponds to the highest pressure during the passage.

Similarly to the observations at Earth, the sheath (region #1) has a variable but intense magnetic field strength, and high proton density and temperature, and it is followed by another region with an even more intense and smoother magnetic field magnitude, and less dense too (region #2). Both of them show elevated temperatures and have a high plasma β. Right after them, an expanding region (#3) with low temperatures and constant magnetic field strength (around 7 nT) can be found. Later on, a period with more or less constant SW speed followed the previous regions, with even lower proton density on average (corresponding to regions #4, #5, #6). These regions are even colder and less dense than the previous ones, their magnetic field is decreasing in strength and is pointing with an inclination of ∼45° with respect to the ecliptic with a main positive (outward) polarity. Consequently, the plasma β in region #6 is lower than the surroundings.

The last part (regions #7, #8) is another expanding regime of the SW, with a very weak magnetic field and similar plasma properties as the previous regions, which draws a higher plasma β. The magnetic field is weak but smooth, going from a south-pointing direction to the nominal behaviour of the Parker spiral within the ecliptic plane.

A few hours after this last region (on March 18 at ∼19:30 UT), another interplanetary shock produced by a different CME arrives at the spacecraft (not indicated in Fig. 6).

A more detailed study of the remote-sensing observations and in situ measurements is performed in the following sections aiming to explain the most probable scenario providing evidence that the structure intercepted at both locations with ∼110° of longitudinal separations corresponds to the same CME that erupted from the Sun on March 13.

3.3. Other locations

We have considered other missions that were also located in the trajectory of the CME or at least in its vicinity and may have been potentially impacted. Nevertheless, they are not shown in the present article due to the complexity of the analysis of their data in addition to evolutionary processes which are out of the scope of the paper.

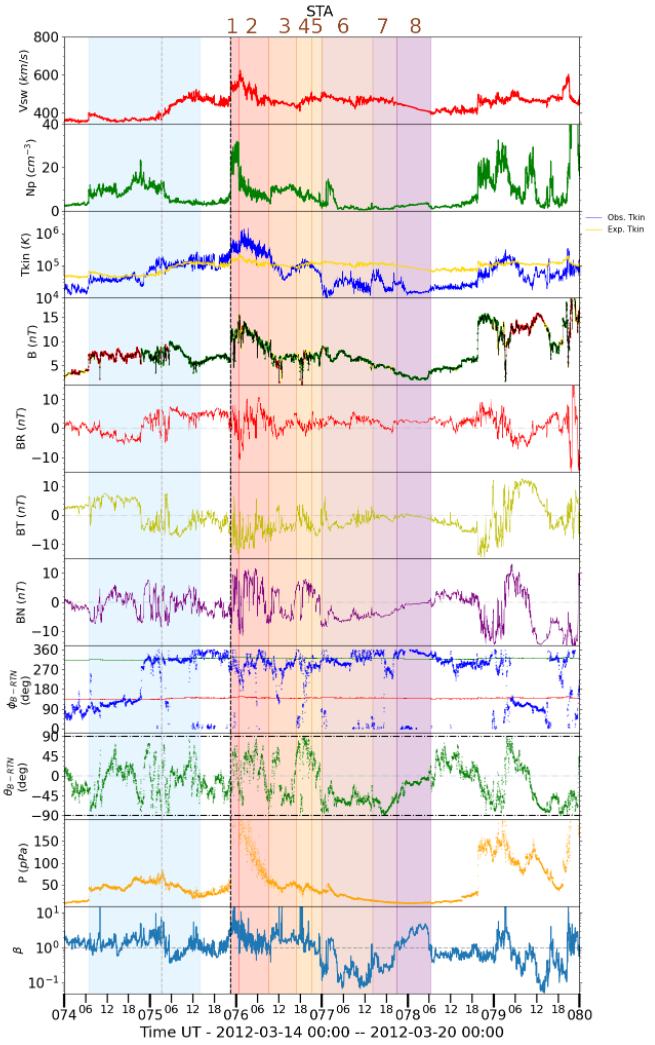

Fig. 6. In situ observations from STEREO-A (March 14, 2012, to March 20, 2012). Blue-shaded area corresponds to the catalogued SIR (see text for more details). Figure follows the same panel format as in Fig. 5.

As a note, one of them was the NASA's Mercury Surface, Space Environment, Geochemistry and Ranging (MESSENGER) mission (Solomon et al. 2001) which was orbiting about Mercury. MESSENGER magnetometer detected the passage of an interplanetary shock at 07:08 UT on March 14 with clear signatures of the passage of a CME at the moment that MESSENGER was in the SW (i.e. outside of Mercury's magnetosphere). At that moment, the spacecraft was located at −31.2° in longitude, 0.4° in latitude and 0.34 au (HEE). Owing to the absence of previous solar events, the observing time (~8.5 h after the eruption) and the MESSENGER location, we suggest that the observed structure corresponds to the same CME under study. Nevertheless, the in situ CME has not been catalogued in previous studies (e.g. Winslow et al. 2015). We note that the longitudinal separation between the site of the parent eruption and the MESSENGER spacecraft was ~85°, which is not inconsistent with the typical width of CME-driven shocks in the interplanetary space (e.g. de Lucas et al. 2011).

4. Data analysis

This section focuses on the morphology and dynamics of the CME from its solar origin to the in situ interplanetary measurements, assuming that the in situ measured structure at Earth and STEREO-A, with a relative separation larger than 100°, corresponds to the same CME. We also show that the structure deflected from an initial considerable out-of-the-ecliptic inclination, to be observed in the ecliptic plane with that separation.

4.1. Reconstruction of the CME near the Sun

For the reconstruction of the size, orientation and kinematics of the structure, the graduated cylindrical shell (GCS) geometrical model has been used (Thernisien 2011) utilising the Python-based PyThea tool (Kouloumvakos et al. 2022). This model assumes a structure similar to a croissant in shape composed of two cones and part of a torus, where different parameters can be adjusted to reconstruct the coronagraph observations, and thus reproduce the leading edge of the structure and obtain, among others, its 3D shape and orientation. A snapshot of the fits applied simultaneously to STEREO-A, STEREO-B and SOHO coronagraph observations is shown in the top row of Fig. 7. The bottom panel of Fig. 7 shows the derived height of the leading edge of the GCS model (i.e. apex) as a function of time, providing a speed of $1982 \pm 75\,\mathrm{km\,s^{-1}}$ when fitted to a first-order function, similar to the one listed in the SOHO/LASCO catalogue (1884–2054 $\mathrm{km\,s^{-1}}$)[12]. The GCS results show an average orientation of ~18° in latitude and ~55° in longitude in Stonyhurst coordinates, a tilt angle of approximately −45° measured counterclockwise positive from the Earth-Sun direction. A similar orientation was obtained in the study Palmerio et al. (2018). Our GCS reconstruction is consistent in longitude and latitude to the AR location on the Sun (N18W64). Also, despite the observed interactions in the lower corona with the surrounding CHs (see Sect. 2.1) and the high-speed streams coming from them, the direction and orientation of the CME did not considerably change in the coronagraphs' field of view.

4.2. CME propagation

Taking into account the arrival time of the shock at both locations (see Sect. 3) and that the eruption appeared on the coronagraphs at ~17:40 UT on March 13 as indicated by the onset of the soft X-rays, the transit time of the CME to reach Earth is ~42.96 h, while for STEREO-A it takes ~52.88 h (both times have been computed considering that the eruption started at the onset time of the soft X-ray emission of the associated flare). Also, according to the GCS reconstruction (see Sect. 4.1), the CME centre (i.e. apex) was propagating ~55° apart from both Earth and STEREO-A. In order to have an estimation of the drag undergone by the CME while propagating in the interplanetary medium, the 1D Drag-Based Model (DBM)[13] has been used (Vršnak et al. 2013; Dumbović et al. 2021), which provides a drag parameter (γ) based on the propagation time. By using the in situ measured SW speed, and assuming that the speed of the structure was the same in both directions and similar to the apex (~2000 $\mathrm{km\,s^{-1}}$), γ obtained for Earth is $0.3753\times10^{7}\ \mathrm{km^{-1}}$, while for STEREO-A is $0.5464\times10^{7}\ \mathrm{km^{-1}}$, suggesting that the structure underwent more drag (~46% more) during its propagation towards STEREO-A than along the Sun-Earth line.

[12] https://cdaw.gsfc.nasa.gov/CME_list/UNIVERSAL/2012_03/univ2012_03.html . The two values 1884 $\mathrm{km\,s^{-1}}$ and 2054 $\mathrm{km\,s^{-1}}$ correspond to a linear and second-order fit to the leading edge of the CME (position angle 286°) versus time as seen in plane-of-sky LASCO/C2 and LASCO/C3 observations.
[13] Available at https://oh.geof.unizg.hr

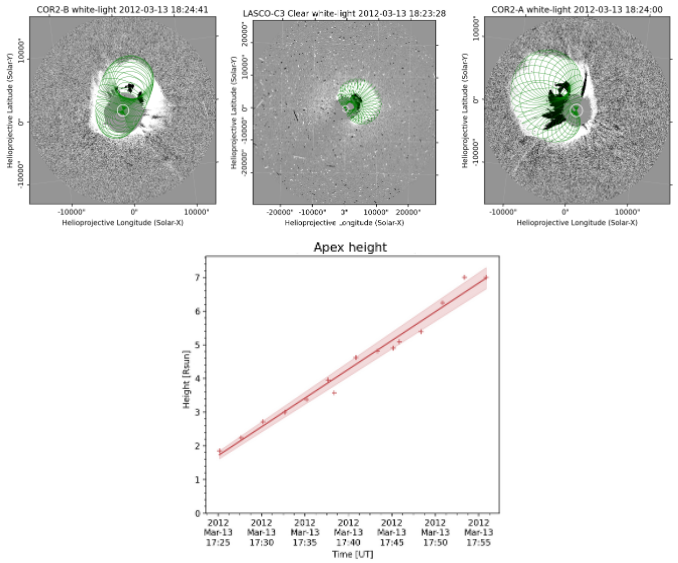

Fig. 7. CME snapshot with GSC reconstruction and calculated speed. Top: running difference images provided by STEREO-B/COR2 (left), SOHO/LASCO/C2 and STEREO-A/COR2 (right) on March 13, 2012, at ~18:24 UT. GCS reconstruction is shown in green. See text for more details. Bottom: height of the apex as a function of time along with linear fit to the data.

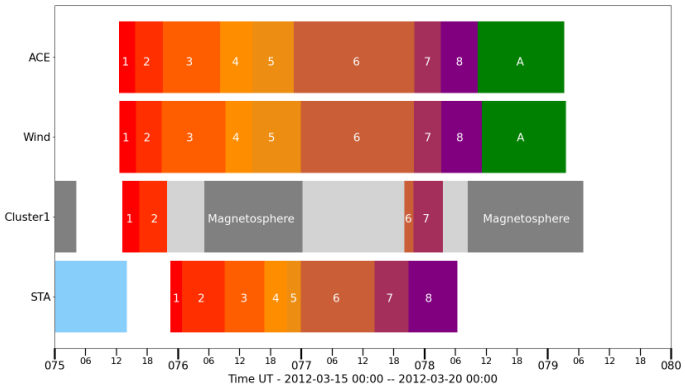

Fig. 8. Timeline of the different identified crossed regions (see Sect. 3 for the definition of the regions) for each spacecraft. Each colour represents each of them (see text for more details). Cluster did not observe the complete sequence of regions due to its entry into the magnetosphere (grey areas).

There are two distinct processes that may explain the difference in drag although the CME propagated with similar longitudinal separation with respect to both spacecraft. These are the swept ambient SW in the Sun-Earth line due to a previous CME (see Sect. 3) and the presence of the SIRs produced by CH2 and CH3. The less-dense conditions left behind the previous CME allow a faster propagation of the CME under study towards Earth (Liu et al. 2014a; Temmer & Nitta 2015), while the presence of SIRs hampers the propagation in STEREO-A direction (Gopalswamy et al. 2009). This can also be appreciated in the higher proton temperature at STEREO-A than at Earth during the first part of the structure, and the difference in density in the upstream SW (~5 cm^{-3} for Earth, ~8 cm^{-3} for STEREO-A), but especially during the transit of the sheath (~9.5 cm^{-3} for Earth, ~27 cm^{-3} for STEREO-A. See Fig. 9), which is more representative of the conditions that the CME experienced during its evolution through the interplanetary medium.

4.3. Longitudinal SW comparison

There is clear evidence suggesting that the plasma measurements at both locations (i.e. at STEREO-A and near-Earth) correspond to different parts of the same structure. In order to prove this, in this Section we perform a more detailed comparison of the plasma properties measured at the subdivided regions of the passage of the CME at both locations.

A timeline of the identified crossed regions is shown in Fig. 8. Table 2 describes the different regions as well as lists the time interval when they were observed, the duration of their passage, and the comparison of the time span with respect to Wind observations. It should be noted that, as described in Sect. 3, those regions do not correspond one-to-one to the traditional identification of the different parts of an in situ measured CME (see Sect. 1), but they are purely based on the SW speed tendency.

As mentioned above, the bulk SW speed profile shows extremely similar behaviours, although there is an almost-systematic offset of ~200 km s^{-1} less in the case of STEREO-A, most likely produced by the interaction of the CME with the preceding SIR (see e.g. Heinemann et al. 2019a, for a similar case). The different regions have been defined based on the discontinuities and changes of tendency of this plasma property. A brief summary of the particular features observed in each region is also described at the bottom of Table 2.

Considering these different regions, an analysis comparing the plasma properties of the passage of the CME through each spacecraft has been performed using normalisation of the time series to initial and end times of observed structures for each region. Figure 9 shows from top to bottom: the bulk SW speed, the components of the velocity in RTN coordinates (V_R, V_T, V_N), the magnetic field magnitude, the components of the magnetic field vector in RTN (B_R, B_T, B_N), and the proton SW density. The red traces indicate STEREO-A observations; dark green, Wind observations; olive green, ACE; and purple, Cluster-4. The SW speed and magnetic field strength exhibit an extraordinary similarity at the different locations and throughout all the regions despite the lower values (by about 200 km s^{-1}) measured by STEREO-A, and some small differences in the field and velocity components. We outline the following details when comparing the measurements of the spacecraft:

– The bulk SW speed obviously displays similar behaviour during all regions, as this parameter was used to select the boundaries. However, a systematic offset of ~200 km s^{-1} between STEREO-A and Earth can be observed.

– Most of the speed corresponds to the radial component, as it is the predominant direction of the SW. In this case, the velocity in the T-N plane would be representative of the lateral expansion of the structure (Owens & Cargill 2004). Regions #2, #3, #7 and #8 show similar behaviour of the velocity components.

– The magnetic field magnitude is very similar during the entire transit, especially during regions #1, #2, #7 and #8.

– The radial and tangential components of the magnetic field vector display both similar values and tendency during region #2, and stable values with similar behaviour during regions #7 and #8.

– Regions #4, #5, #6 present fluctuating velocity components and less correlated magnetic field strength and

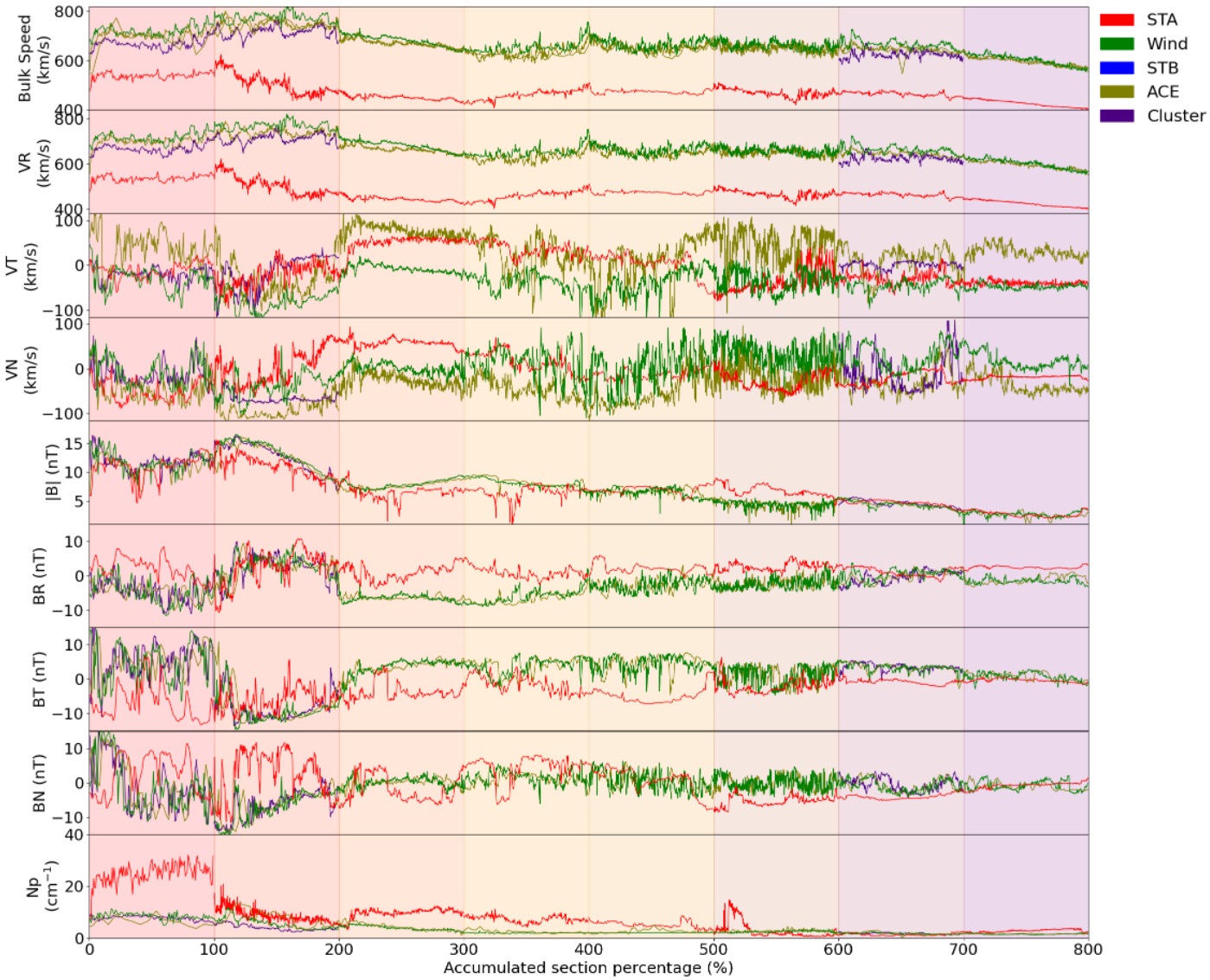

Fig. 9. Comparison of the plasma and magnetic field properties through the different regions. From top to bottom: plasma velocity (magnitude and RTN components), magnetic field (magnitude and RTN components), and proton density. *X*-axis corresponds to the cumulative percentage of data points of the different regions. Each shade colour corresponds to the different regions utilised in previous figures. All data are resampled to a 1-min cadence. See text for more details.

components. These differences, together with the similarities of the surrounding areas, suggest that these regions (#4, #5, #6) are under different plasma conditions. Also, it supports the idea that at both locations (i.e. STEREO-A and Earth), the main structure is being crossed twice (in, out, in. See Sect. 5 for more details).

– In all regions, the proton density shows a clear difference between STEREO-A and Wind, being almost systematically ∼3 times greater at STEREO-A, most likely due to the interaction with the SIR, which also slows down the CME propagation in the Sun–STEREO-A direction.

As shown in Fig. 9, there are certain parts during the transit of the CME through the spacecraft with such similarity that evinces the presence of the same structure crossing STEREO-A and near-Earth observatories despite their notable separation.

In order to quantify the similarity between the SW speed, velocity components, magnetic field magnitude, magnetic field components, and SW density at STEREO-A and near-Earth in each region of the CME passage, Fig. 10 shows the Pearson correlation coefficient between them computed for each region. The calculation has been performed correlating the observations of each in situ parameter from STEREO-A and near-Earth spacecraft. Then, the largest correlation out of the three combinations (STEREO-A and Wind, STEREO-A and ACE, or STEREO-A and Cluster) has been selected. Despite the long separation between STEREO-A and near-Earth spacecraft, local particularities, and the evolutionary processes undergone by the structure along the different directions (apart from the instrumental differences and cadences), the speed and magnetic field strength are correlated with a Pearson correlation coefficient greater than 0.5 for most of the crossed regions. In particular, the magnetic field displays a better correlation during the front (regions #1 and #2) and rear portions of the CME (regions #7 and #8), while the SW speed does for regions #1, #3, #4, #7 and #8. Although the main property used for selecting the boundaries of each region was the bulk speed, the correlation is higher for the magnetic field. The above results suggest that the structure is magnetically coherent despite the local plasma properties.

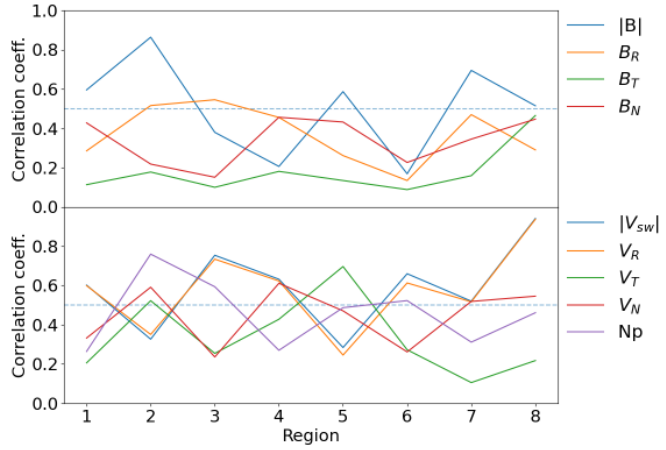

Fig. 10. Greatest Pearson correlation coefficient values found between STEREO-A and near-Earth spacecraft observations for each defined sector of the parameters shown in Fig. 9.

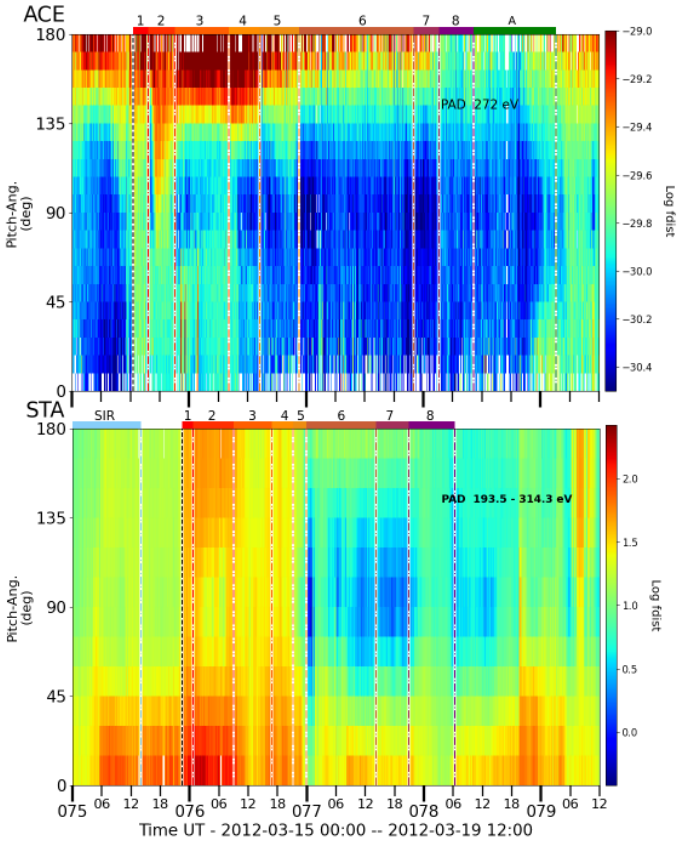

Fig. 11. Top: suprathermal electron PADs (time series of the distribution function, Fdist, with respect to the magnetic field angle) for the 272 eV energy channel measured by ACE/SWEPAM from March 14, 2012, to March 19, 2012, at 12:00 UT. Bottom: in situ PADs of the suprathermal electrons from 193.5 to 314.3 eV measured by STEREO-A/SWEA for the same period. Dashed lines and top colour bars represent the different defined regions. See text for more details.

Apart from the difference in time between ACE and Wind observations of the different features of the bulk speed profile (that can be more than one hour apart; see Table 2), there is also a difference in the velocity components despite their relatively small separation (see Fig. 9). This may indicate that the expansion of the structure (regions #3 and #8) is occurring differently at both positions, probably due differences in the proximity of both spacecraft to the central part of the expanding local plasma (i.e. the impact parameter of both spacecraft; see e.g. Dasso et al. 2007; Démoulin et al. 2008, for details). The quasi-stable values and the increment of the tangential (T) and normal (N) components with respect to the radial (R) could be also indicative of the existence of a transit through the leg of the structure (as derived from Démoulin et al. 2008).

Besides, considering the interaction of the structure with the locally encountered upstream ambient SW, the piled-up plasma in the sheath (region #1) presents a similar behaviour and an unexpectedly high correlation, considering the completely different conditions of the SW that the structure suffered while propagating to the observatories.

4.4. Suprathermal electron pitch-angle distributions

Suprathermal electrons are a good tracer of the interplanetary magnetic field topology and properties, especially when comparing their pitch-angle with respect to the direction of the magnetic field. Figure 11 top (bottom) panel shows the 272 eV (193.5–314.3 eV) PADs obtained from ACE/SWEPAM (STEREO-A/SWEA) measurements from 00:00 UT on March 15 to 12:00 UT on March 19. Different colour blocks on top of each panel and dashed lines correspond to the previously defined regions (see Sect. 4.3). The sporadic peaks (and floor) are intentionally saturated, as their high (low) intensity smears the visual contrast of the rest of the period.

Focusing on the top panel, ACE observed a simple *strahl* coming from the anti-parallel direction before the arrival of the CME. The width of the *strahl* becomes broader while approaching the CME shock. Within region #1, the PAD is nearly isotropic, which is a typical signature of the sheaths (e.g. Carcaboso et al. 2020). Region #2 displays periods of BDE especially at the beginning and the *strahl* electron width coming from 180° becomes larger until the end of the period. This behaviour suggests there is a still linked-to-the-Sun tube (i.e., a FR) of particles which is undergoing local disturbances that broaden the *strahl* predominantly coming from 180° (see e.g. Horaites et al. 2018, for potential sources of scattering). The reason underneath this observation may result from a local feature within region #2 because the smoothness of the magnetic field, in this overall expanding region, will cause the electrons to focus more easily than in the ambient SW due to adiabatic expansion (Anderson et al. 2012).

The top panel of Fig. 11 shows that region #3 was characterised by clear BDEs, with the electrons coming from 0° presenting larger width but less intensity than those coming from 180°. The intensities of the electrons coming from 0° decrease in region #4, and the width of those coming from 180° increases. Region #5 has a similar behaviour to region #2 in the predominant *strahl*. Region #6 shows sporadic periods of BDE and isotropy, and predominant simple *strahl*, which suggests that there is a mix of open, closed, and completely detached magnetic field lines. Overall, region #7 shows a simple *strahl* narrower than in previous regions. Region #8 shows a weaker intensity of those electrons coming from 180°. Also, it displays some intermittent periods of BDE and isotropy. Finally, region A shows simple *strahl* with some isotropic periods. At the end, the counterstreaming electrons are becoming clearer due to the proximity of the upcoming SIR.

The whole transit of ACE through the structure presents periods of more or less clear BDEs (sometimes longer,

sometimes patchy behaviour), and systematically, a *strahl* population with pitch angles ~0° less intense than the population with pitch angles ~180°. This could be related to having a flank crossing close to one leg of the structure, which apparently owns a preferential negative (inward) direction (see examples in Kahler et al. 1996). In addition, it agrees with the remotely observed handedness (left) previously mentioned in Sect. 2.1 and reported by Palmerio et al. (2018), having the more intense *strahl* population in the opposite direction than the dominant magnetic field. As discussed below, this is consistent with the spacecraft crossing the east leg of the structure. On the other hand, the absence of BDEs may be an indicator that only part of the CME remained magnetically closed, whereas the other parts were eroded (possibly due to interaction with the fast SW) or originally were open magnetic field lines (e.g. Winslow et al. 2016; Carcaboso et al. 2020).

The bottom panel of Fig. 11 shows STEREO-A observations. The blue-shaded period marked in Fig. 6 is also in the bottom panel of Fig. 11, and corresponds to the passage of a SIR that started to cross STEREO-A on March 14, as identified by Jian et al. (2019). The difference between the *strahl* peak and the background is not as pronounced as it is during the passage of the high-speed stream right before the arrival of the CME. The *strahl* population of the suprathermal electrons follows the polarity of the nominal Parker spiral (positive). Within the CME passage at STEREO-A, region #1 displays isotropic electron PADs, similarly to ACE; region #2 shows clear BDEs, with some periods of isotropy; the boundary between region #2 and #3 is completely isotropic, and region #3 shows a smeared *strahl* population, reaching widths greater than 90° and reaching the complete isotropy by the end, indicating the presence of magnetic in situ reconnections (e.g. Gosling et al. 2005); region #4 shows a similar behaviour, but with clearer isotropy; region #5 gradually shows greater BDEs, and regions #6 and #7 shows the clearest BDE period, with higher intensities and *strahl* widths at 0° than 180°; finally, region #8 also shows BDE but with less gradient between peaks and background.

The overall tendency of the electron PADs at STEREO-A during the transit of the CME is the clear presence of BDEs with a predominant peak intensity parallel to the magnetic field. Assuming that the magnetic field is predominantly axial, and STEREO-A crossed closer to the west leg of the CME, this behaviour supports the idea that the handedness derived from remote sensing observations (left-handedness) previously reported by Palmerio et al. (2018) also matches the one observed in situ. In this case, the peak intensity in the BDEs could be also indicative of the proximity to the different legs of the structure (Kahler et al. 1996). While STEREO-A observes a more intense flux coming from the parallel direction (pitch-angle ~0°), near-Earth measurements show a predominant higher peak with pitch angles at ~180° (anti-parallel to the magnetic field).

Considering the longitudinal separation between STEREO-A and Earth, the suprathermal electrons would take a longer time to travel from one location to the other than the actual passage time of each defined CME region over each spacecraft. As a reference, a completely field-aligned electron of 300 eV would take approximately 13.5 h to travel 1.62 au, which corresponds to the absolute distance between STEREO-A and Earth (actual magnetic field path-length would be longer in a FR structure, and the particle would have an inherent gyroradius). Despite this fact, there are remarkable similarities in their PADs at both locations, suggesting that the transport conditions that those electrons may have experienced are similar regardless of having travelled completely different paths. The different regions (purely defined by the changes in the SW speed tendencies) are strongly linked to the behaviour of the PADs.

5. Possible scenario

Figure 12 sketches the envisaged scenario of the CME structure and the SW conditions in the interplanetary medium during the event. This scenario is based on the measurements and the performed analysis and represents the most plausible reconstruction according to our assessment. However, other alternative interpretations could exist. The top panel represents a view from the north of the ecliptic and the bottom panel a view from the nose of the structure directed between Earth (green sphere) and STEREO-A (red sphere). Earth would cross the east flank of the CME ~10 h before STEREO-A, which would cross the west flank. At the time Earth crosses the shock and sheath of the structure, STEREO-A is crossing a high-speed stream (indicated by the greenish tube in Fig. 12) likely originated from CH3 (or the combination of CH2 and CH3).

According to the GCS reconstructions, the CME originated ~55° in longitude between both spacecraft whereas the half angle of the structure was ~50°. The structure was also very inclined (~45° with respect to the ecliptic plane), so in order to cover a large longitudinal span over the ecliptic plane later at 1 au, the structure had to widely expand in that direction, rotate and/or bend to cover that space. Shock orientations (at Earth pointing southwest, and at STEREO-A pointing west) indicate that the deformation/rotation was very likely.

There are also indications that the portion of the CME directed towards STEREO-A would have started to interact with the high-speed streams produced by CH2 and CH3 at closer radial distances, such as the presence of higher densities at STEREO-A (3 times greater than at Earth), the speed was ~200 km s^{-1} lower, as well as the duration of the passage (shorter in the case of STEREO-A), suggesting that the structure was likely more compressed on average in that portion of the CME.

The similarities of different plasma properties at the two locations (bulk SW speed, behaviour of the velocity components, magnetic field strength, PADs...) suggest that at least the three first regions (#1, #2, #3) and the two last regions (#7, #8) correspond to the same structure, which matches with the CME originated on March 13 at 17:12 UT, while regions #4 and #5 display mixed signatures of ambient SW and magnetic obstacle, with evidence of local reconnection as indicated by, among others, the observed suprathermal electrons PADs. Additionally, region #6 in the case of Earth's observations does not show clear signatures of being part of the core of the structure, while for STEREO-A, there is a clear inclined and smooth magnetic field, with low temperatures, low plasma β and BDEs, for which it could be identified as a MC.

This scenario differs from what Tsurutani et al. (2014) found for this event based only on near-Earth in situ observations (see Fig. 5 in that article). That study proposes that from region #4 to #8, the SW presents high-speed stream signatures. From our observations, we did not find clear evidence for the source of this fast SW, but the one produced by the CME itself.

6. Summary

A CME associated with a M7.9 flare was released on March 13, 2012, with a speed of ~2000 km s^{-1}, and an inclination of approximately 45°. The CME started propagating outwards from the Sun in a direction 55° east from Earth, that is,

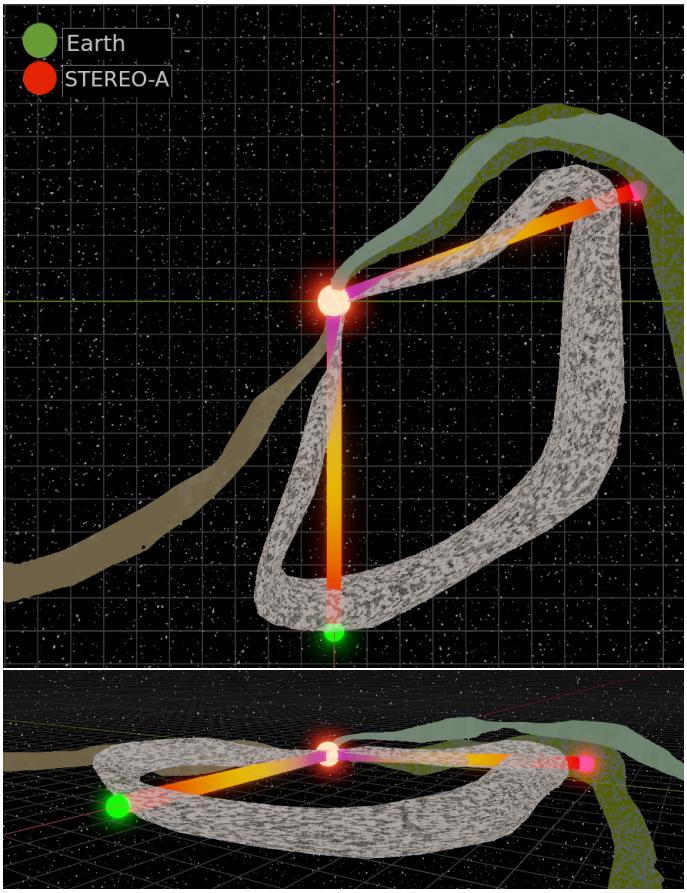

Fig. 12. Proposed scenario based on the observations. Spacecraft and structures are located at the moment of the encounter with Wind. At that moment, STEREO-A was found in the high-speed stream. The green and brown traces represent the high-speed streams generated by CH2/CH3 and CH1, respectively. Colour bars represent the radial cross through the conditions of the SW following the same format as Figs. 8 and 9.

between Earth and STEREO-A which were separated by ∼110° apart from each other in longitude. The AR was surrounded by three CHs. At least one of them interacted with the CME while it propagated away from the Sun, hampering its propagation towards STEREO-A.

The GCS reconstruction and the derived kinematics seem to be consistent with the arrival time of the CME at both locations and the in situ measurements at ∼1 au. There is no evidence of the presence of other CMEs of similar magnitude 24 h prior to and after the CME, observed by LASCO and SECCHI coronagraphs, which erupted on March 13, 2012, at ∼17:30 UT. This can be assured thanks to the orbital position of the two STEREOs and Earth, which allowed a 360° visual coverage of the Sun.

The DBM model suggests that although it is the same structure, there is a ∼46% more drag towards STEREO-A than towards Earth, most likely because of two complementing effects: a previous CME towards Earth swept the SW in that direction, and the presence of the high-speed streams produced by CH2 and CH3.

The computation of the shock parameters presented indicates that the shock normal vector at Wind location was pointing southwest and, at STEREO-A location, it was contained in the ecliptic plane pointing west.

Despite the large longitudinal separation and initial inclination of the structure, the bulk SW speed and magnetic field magnitude displayed almost identical profiles on near-Earth observatories and STEREO-A, suggesting that the observed CME is the same structure at both spatial locations. STEREO-A transited the west flank, while Earth did it through the east one. The in situ observations show opposite field polarity on STEREO-A compared to Wind/ACE (negative for Earth's and positive for STEREO-A's), and the suprathermal electron PAD during the BDE periods supports the in situ left-handedness, matching the one reported by Palmerio et al. (2018) using remote sensing observations. Also, the higher intensity of the *strahl* population at 0° on STEREO-A, and at 180° on Earth's observation, during the BDE periods could indicate the proximity to the magnetic foot point of the CME.

As it can be derived from the timeline and the Δt column in Table 2, some parts of the structure seem to have transits of different duration depending on the observer (even with the very-close-to-each-other Wind and ACE). This has significant implications for our understanding of the CMEs, as most of the studies are based on just single point observations.

Despite not having clear smooth magnetic field rotation in the STEREO-A region #2, there are pronounced BDEs, similar to those observed at ACE, but with the highest peak in the opposite direction (suggesting that both spacecraft intercepted the flanks of the CME close to the respective legs, as mentioned above). Assuming that the regions are part of the same structure and that no remarkable evolutionary processes have happened (which may have resulted in a different imprint in the PADs), the identification of what traditionally has been called FR extends further than the actual helical magnetic field, which would correspond to the magnetic obstacle or region #3.

A geomagnetic storm with $Kp > 5$ was produced while Earth was crossing a strong negative B_z component. The geomagnetic effects ($Kp \sim 4$) lasted until the end of the passage of the structure by Earth. However, previous catalogues reported a shorter in situ CME passage.

7. Conclusion and discussion

The main conclusions of this work can be stated as follows:

1. There is clear evidence of having the same CME observed by 110° separation although its initial inclination was ∼45°. Based on these observational facts, we propose a scenario (Sect. 5) in which an originally highly inclined wide CME deformed and/or rotated in such a way that it was observed near its legs by spacecraft in the ecliptic plane separated by >100° in longitude.
2. The structure interacts with at least one of the high-speed streams produced by the west CHs (CH2, CH3) surrounding the AR, which probably caused the deformation and deceleration of the structure in the STEREO-A direction.
3. The piled-up plasma observed in the sheath (region #1) has an unexpectedly extraordinary correlation in the magnetic field strength at the two locations separated by 110° in longitude. This plasma is supposedly a mixture of the CME and the local ambient SW compressed downstream the shock. Despite the ambient conditions at both locations were different, the similarities in the magnetic field strength require a deeper analysis.
4. The in situ observations reveal that at both locations each spacecraft crossed the respective flanks of the CME, then ambient SW, and finally the legs' proximity of the CME. In the case of STEREO-A, the cross through the leg is more

evident than for near-Earth spacecraft (see Fig. 12, which sketches the proposed scenario).
5. We found no clear evidence for a potential source for a high-speed stream crossing Earth during the period from March 16 to March 18 as suggested by Tsurutani et al. (2014).

The similarities of the structure regardless of the large angular separation are evidenced, in contrast to previous studies, such as the case-study event analysed by Lugaz et al. (2022), where less clear correlations are found despite the spacecraft locations observing the CME were closer to each other. This shows that the factors that determine each particular observation (i.e. how the spacecraft intercepts the CME, the morphology and evolutionary processes of the CME, SW conditions, etc.) play the main role in the interpretation of the observations and derived scientific results . On the other side, having relatively close proximity does not assure similar measurements. They may significantly differ more than one hour in the definition of each region based on the bulk speed (e.g. see column Δt for near-Earth spacecraft on Table 2). These differences play a very relevant role in the scientific explanation, and thus in our understanding of the large-scale structures, such as the CMEs are. Even with the extensive catalogues available, the use of single spacecraft data during the transit of the CMEs implies that the derived interpretations may suffer large inconsistencies. Nevertheless, the use of the available multipoint measurements helps, and it is even required, to support the different encountered scenarios.

This case study opens up questions about our current view of the CME longitudinal spread and its evolution in the interplanetary space, pointing out the need to find more examples of widespread CMEs and analyse them. Such analysis will help us understand the eruption, evolution and global topology of CMEs, as well as improve our modelling efforts.

Acknowledgements. The authors acknowledge the open policy of the data for the different missions. We acknowledge use of NASA/GSFC's Space Physics Data Facility's CDAWeb service. FC acknowledges the financial support by an appointment to the NASA Postdoctoral Program at NASA Goddard Space Flight Center, administered by Oak Ridge Associated Universities through a contract with NASA and the support of the Solar Orbiter mission. FC and LKJ thank the support of the STEREO mission. MD acknowledges the support by the Croatian Science Foundation under the project IP-2020-02-9893 (ICOHOSS). RGH acknowledges the financial support of the Spanish Ministerio de Ciencia Innovación y Universidades Project PID2019-104863RBI00/AEI/10.13039/501100011033 and by the European Union's Horizon 2020 research and innovation program under grant agreement No. 101004159 (SERPENTINE). SGH acknowledges funding by the Austrian Science Fund (FWF): Erwin-Schrödinger fellowship J-4560. LKJ and TNC are supported by HGI-Open grant 80NSSC23K0447. This work has been possible thanks to the scientific discussions within the LASSOS-Goddard group. FC thanks Benjamin Lynch, Angelos Vourlidas and Andreas Weiss for the discussions, and also the referee for their feedback.

References

Acuña, M. H., Curtis, D., Scheifele, J. L., et al. 2008, Space Sci. Rev., 136, 203
Anderson, B. R., Skoug, R. M., Steinberg, J. T., & McComas, D. J. 2012, J. Geophys. Res. (Space Phys.), 117
Balogh, A., Carr, C. M., Acuña, M. H., et al. 2001, Ann. Geophys., 19, 1207
Brueckner, G. E., Howard, R. A., Koomen, M. J., et al. 1995, Sol. Phys., 162, 357
Bürgi, A. 1992, Sol. Wind Seven, 333
Burlaga, L., Sittler, E., Mariani, F., & Schwenn, R. 1981, J. Geophys. Res., 86, 6673
Carcaboso, F., Gómez-Herrero, R., Espinosa Lara, F., et al. 2020, A&A, 635, A79
Cargill, P. J., Chen, J., Spicer, D. S., & Zalesak, S. T. 1996, J. Geophys. Res., 101, 4855
Chen, C., Liu, Y. D., Wang, R., et al. 2019, ApJ, 884, 90
Chen, C., Liu, Y. D., & Zhu, B. 2022, ApJ, 937, 44
Dasso, S., Nakwacki, M. S., Démoulin, P., & Mandrini, C. H. 2007, Sol. Phys., 244, 115
Davies, J., Harrison, R., Rouillard, A., et al. 2009, Geophys. Res. Lett., 36
de Lucas, A., Schwenn, R., dal Lago, A., Marsch, E., & Clúa de Gonzalez, A. L. 2011, J. Atmos. Sol.-Terr. Phys., 73, 1281
Démoulin, P., Nakwacki, M. S., Dasso, S., & Mandrini, C. H. 2008, Sol. Phys., 250, 347
Dhakal, S. K., Zhang, J., Vemareddy, P., & Karna, N. 2020, ApJ, 901, 40
Domingo, V., Fleck, B., & Poland, A. I. 1995, Sol. Phys., 162, 1
Dumbović, M., Čalogović, J., Martinić, K., et al. 2021, Front. Astron. Space Sci., 8
Elliott, H. A., Henney, C. J., McComas, D. J., Smith, C. W., & Vasquez, B. J. 2012, J. Geophys. Res. (Space Phys.), 117
Escoubet, C. P., Fehringer, M., & Goldstein, M. 2001, Ann. Geophys., 19, 1197
Eyles, C. J., Harrison, R. A., Davis, C. J., et al. 2009, Sol. Phys., 254, 387
Feng, L., Lu, L., Inhester, B., et al. 2020, Sol. Phys., 295, 141
Galvin, A. B., Kistler, L. M., Popecki, M. A., et al. 2008, Space Sci. Rev., 136, 437
Geyer, P., Dumbovic, M., Temmer, M., et al. 2023, A&A, 672, A168
Gloeckler, G., Cain, J., Ipavich, F. M., et al. 1998, Space. Sci. Rev., 86, 497
Gold, R. E., Krimigis, S. M., Hawkins, S. E., et al. 1998, Space. Sci. Rev., 86, 541
Gopalswamy, N., Mäkelä, P., Xie, H., Akiyama, S., & Yashiro, S. 2009, J. Geophys. Res. (Space Phys.), 114, A00A22
Gosling, J. T., Baker, D. N., Bame, S. J., et al. 1987, J. Geophys. Res., 92, 8519
Gosling, J. T., Skoug, R. M., McComas, D. J., & Smith, C. W. 2005, Geophys. Res. Lett., 32
Harker, B. J., & Pevtsov, A. A. 2013, ApJ, 778, 175
He, W., Liu, Y. D., Hu, H., Wang, R., & Zhao, X. 2018, ApJ, 860, 78
Heinemann, S. G., Hofmeister, S. J., Veronig, A. M., & Temmer, M. 2018a, ApJ, 863, 29
Heinemann, S. G., Temmer, M., Hofmeister, S. J., Veronig, A. M., & Vennerstrøm, S. 2018b, ApJ, 861, 151
Heinemann, S. G., Temmer, M., Farrugia, C. J., et al. 2019a, Sol. Phys., 294, 121
Heinemann, S. G., Temmer, M., Heinemann, N., et al. 2019b, Sol. Phys., 294, 144
Horaites, K., Boldyrev, S., Wilson, L. B., Viñas, A. F., & Merka, J. 2018, MNRAS, 474, 115
Howard, R. A., Moses, J. D., Socker, D. G., et al. 2002, Adv. Space Res., 29, 2017
Hudson, M. K., Engel, M. A., Kress, B. T., et al. 2023, J. Geophys. Res. (Space Phys.), 128, e2022JA031106
Ipavich, F. M., Galvin, A. B., Gloeckler, G., Scholer, M., & Hovestadt, D. 1981, J. Geophys. Res.: Space Phys., 86, 4337
Jaeggli, S. A., & Norton, A. A. 2016, ApJ, 820, L11
Jian, L., Russell, C. T., Luhmann, J. G., & Skoug, R. M. 2006a, Sol. Phys., 239, 337
Jian, L. K., Russell, C. T., Luhmann, J. G., & Skoug, R. M. 2006b, Sol. Phys., 239, 393
Jian, L. K., Russell, C. T., Luhmann, J. G., et al. 2013, in Solar Wind 13, eds. G. P. Zank, J. Borovsky, R. Bruno, et al., AIP Conf. Ser., 1539, 191
Jian, L. K., Russell, C. T., Luhmann, J. G., & Galvin, A. B. 2018, ApJ, 855, 114
Jian, L. K., Luhmann, J. G., Russell, C. T., & Galvin, A. B. 2019, Sol. Phys., 294, 31
Kahler, S. W., Crocker, N. U., & Gosling, J. T. 1996, J. Geophys. Res. (Space Phys.), 101, 24373
Kaiser, M. L., Kucera, T. A., Davila, J. M., et al. 2008, Space Sci. Rev., 136, 5
Kouloumvakos, A., Rodríguez-García, L., Gieseler, J., et al. 2022, Front. Astron. Space Sci., 9, 974137
Koval, A., & Szabo, A. 2008, J. Geophys. Res. (Space Phys.), 113, A10110
Krall, N. 1997, Adv. Space Res., 20, 715
Lario, D., Ho, G. C., Roelof, E. C., Anderson, B. J., & Korth, H. 2013, J. Geophys. Res. (Space Phys.), 118, 63
Lemen, J. R., Title, A. M., Akin, D. J., et al. 2012, Sol. Phys., 275, 17
Lepping, R. P., Acũna, M. H., Burlaga, L. F., et al. 1995, Space. Sci. Rev., 71, 207
Lin, R. P., Anderson, K. A., Ashford, S., et al. 1995, Space. Sci. Rev., 71, 125
Liu, Y., Richardson, J. D., Belcher, J. W., Kasper, J. C., & Skoug, R. M. 2006, J. Geophys. Res. (Space Phys.), 111, A09108
Liu, Y., Luhmann, J. G., Müller-Mellin, R., et al. 2008, ApJ, 689, 563
Liu, Y. D., Luhmann, J. G., Lugaz, N., et al. 2013, ApJ, 769, 45
Liu, Y. D., Luhmann, J. G., Kajdič, P., et al. 2014a, Nat. Commun., 5, 3481
Liu, Y. D., Richardson, J. D., Wang, C., & Luhmann, J. G. 2014b, ApJ, 788, L28
Lopez, R. E. 1987, J. Geophys. Res., 92, 11189
Lugaz, N., Salman, T. M., Zhuang, B., et al. 2022, ApJ, 929, 149
Luhmann, J. G., Curtis, D. W., Schroeder, P., et al. 2008, Space Sci. Rev., 136, 117
McComas, D., Bame, S., Barker, P., et al. 1998, Space Sci. Rev., 86, 563

Möstl, C., Farrugia, C. J., Miklenic, C., et al. 2009, J. Geophys. Res. (Space Phys.), 114, A04102
Mullan, D. J., & Smith, C. W. 2006, Sol. Phys., 234, 325
Newbury, J. A. 1996, Eos, Trans. Am. Geophys. Union, 77, 471
Nieves-Chinchilla, T., Vourlidas, A., Raymond, J. C., et al. 2018, Sol. Phys., 293, 25
Nieves-Chinchilla, T., Jian, L. K., Balmaceda, L., et al. 2019, Sol. Phys., 294, 89
Ogilvie, K. W., & Desch, M. D. 1997, Adv. Space Res., 20, 559
Ogilvie, K. W., Chornay, D. J., Fritzenreiter, R. J., et al. 1995, Space. Sci. Rev., 71, 55
Owens, M., & Cargill, P. 2004, Ann. Geophys., 22, 4397
Palmerio, E., Kilpua, E. K. J., James, A. W., et al. 2017, Sol. Phys., 292, 39
Palmerio, E., Kilpua, E. K. J., Möstl, C., et al. 2018, Space Weather, 16, 442
Patsourakos, S., Georgoulis, M. K., Vourlidas, A., et al. 2016, ApJ, 817, 14
Pesnell, W. D., Thompson, B. J., & Chamberlin, P. 2011, The Solar Dynamics Observatory (Springer), 3
Rème, H., Aoustin, C., Bosqued, J. M., et al. 2001, Ann. Geophys., 19, 1303
Richardson, I. G., & Cane, H. V. 2010, Sol. Phys., 264, 189
Richardson, J. D., Paularena, K. I., Wang, C., & Burlaga, L. F. 2002, J. Geophys. Res. (Space Phys.), 107, SSH 1
Riley, P., & Crooker, N. U. 2004, ApJ, 600, 1035
Rodriguez, L., Masías-Meza, J. J., Dasso, S., et al. 2016, Sol. Phys., 291, 2145
Rodríguez-García, L., Gómez-Herrero, R., Zouganelis, I., et al. 2021, A&A, 653, A137
Rouillard, A. 2011, J. Atmos. Sol.-Terr. Phys., 73, 1201
Salman, T. M., Lugaz, N., Farrugia, C. J., et al. 2020, ApJ, 904, 177
Sauvaud, J.-A., Larson, D., Aoustin, C., et al. 2008, Space Sci. Rev., 136, 227
Scolini, C., Winslow, R. M., Lugaz, N., & Poedts, S. 2023, ApJ, 944, 46
Smith, C. W., L'Heureux, J., Ness, N. F., et al. 1998, Space Sci. Rev., 86, 613
Solomon, S. C., McNutt, R. L., Gold, R. E., et al. 2001, Planet. Space Sci., 49, 1445
Soni, S. L., Selvakumaran, R., & Thampi, R. S. 2023, Front. Astron. Space Sci., 9, 441
Stone, E. C., Frandsen, A., Mewaldt, R., et al. 1998, Space Sci. Rev., 86, 1
Su, Y., van Ballegooijen, A., McCauley, P., et al. 2015, ApJ, 807, 144
Temmer, M., & Bothmer, V. 2022, A&A, 665, A70
Temmer, M., & Nitta, N. V. 2015, Sol. Phys., 290, 919
Temmer, M., Reiss, M. A., Nikolic, L., Hofmeister, S. J., & Veronig, A. M. 2017, ApJ, 835, 141
Thernisien, A. 2011, ApJS, 194, 33
Thompson, W. T., Davila, J. M., Fisher, R. R., et al. 2003, in Innovative Telescopes and Instrumentation for Solar Astrophysics, eds. S. L. Keil, & S. V. Avakyan, SPIE Conf. Ser., 4853, 1
Tsurutani, B. T., Echer, E., Shibata, K., et al. 2014, J. Space Weather Space Clim., 4, A02
Viñas, A. F., & Scudder, J. D. 1986, J. Geophys. Res. (Space Phys.), 91, 39
Vourlidas, A., Balmaceda, L. A., Stenborg, G., & Dal Lago, A. 2017, ApJ, 838, 141
Vršnak, B. 2001, Sol. Phys., 202, 173
Vršnak, B., & Gopalswamy, N. 2002, J. Geophys. Res. (Space Phys.), 107, 1019
Vršnak, B., Poletto, G., Vujić, E., et al. 2009, A&A, 499, 905
Vršnak, B., Žic, T., Vrbanec, D., et al. 2013, Sol. Phys., 285, 295
Wilson, III., L. B. 2022, https://doi.org/10.5281/zenodo.6141586
Wilson, L. B., III, Brosius, A. L., Gopalswamy, N., et al. 2021, Rev. Geophys., 59, e2020RG000714
Winslow, R. M., Lugaz, N., Philpott, L. C., et al. 2015, J. Geophys. Res. (Space Phys.), 120, 6101
Winslow, R. M., Lugaz, N., Schwadron, N. A., et al. 2016, J. Geophys. Res. (Space Phys.), 121, 6092
Winslow, R. M., Scolini, C., Jian, L. K., et al. 2022, Front. Astron. Space Sci., 9
Witasse, O., Sánchez-Cano, B., Mays, M. L., et al. 2017, J. Geophys. Res. (Space Phys.), 122, 7865
Zurbuchen, T. H., & Richardson, I. G. 2006, Space Sci. Rev., 123, 31

Appendix A: Missions and instruments

The instruments utilised in this study are listed below. On the one hand, the remote-sensing instrumentation listed by each mission was:

- **Solar Dynamics Observatory** (SDO, Pesnell et al. 2011): Atmospheric Imaging Assembly (AIA, Lemen et al. 2012).
- **Solar and Heliospheric Observatory** (SOHO, Domingo et al. 1995): Large Angle Spectroscopic Coronagraph (LASCO, Brueckner et al. 1995).
- **STEREO**: Heliospheric Imager (HI, Eyles et al. 2009), Extreme UltraViolet Imager (EUVI), and the two coronagraphs (COR1, COR2), all being part of the suite Sun-Earth Connection Coronal and Heliospheric Investigation (SECCHI, Thompson et al. 2003; Howard et al. 2002).

On the other hand, the in situ instrumentation was:

- **ACE**: The Electron, Proton, and Alpha Monitor (EPAM, Gold et al. 1998), the Solar Wind Electron Proton Alpha Monitor (SWEPAM, McComas et al. 1998), the Solar Wind Ion Composition Spectrometer (SWICS, Gloeckler et al. 1998), and the magnetometer of the Magnetic Fields Experiment (Smith et al. 1998).
- **Cluster**: The magnetometer (Balogh et al. 2001) and the Cluster Ion Spectrometry experiment (Rème et al. 2001).
- **STEREO-A**: The suite of instruments of the In situ Measurements of Particles And CME Transients (IMPACT, Luhmann et al. 2008), particularly the instruments Solar Wind Electron Analyzer (SWEA, Sauvaud et al. 2008) and the magnetometer (Acuña et al. 2008), and the Plasma and Suprathermal Ion Composition (PLASTIC, Galvin et al. 2008).
- **Wind**: The Solar Wind Experiment (SWE, Ogilvie et al. 1995), the Magnetic Field Investigation (MFI, Lepping et al. 1995), and the 3-D Plasma and Energetic Particle Investigation (3DP, Lin et al. 1995).